

Joule heating effects on electrokinetic flows with conductivity gradients

Le Song,^{1,2} Liandong Yu,^{1,3*} Christian Brumme,² Ryan Shaw,² Cheng Zhang,⁴ and Xiangchun Xuan²

¹School of Instrument Science and Opto-electronic Engineering, Hefei University of Technology, Hefei 230009, China

²Department of Mechanical Engineering, Clemson University, Clemson, SC 29634-0921, USA

³College of Controlling Science and Engineering, China University of Petroleum, Qingdao 257061, China

⁴Department of Mechanical Engineering, University of West Florida, Pensacola, FL 32514, USA

Correspondence: Professor Xiangchun Xuan, Department of Mechanical Engineering, Clemson University, Clemson, SC 29634-0921, USA. **E-mail:** xcxuan@clemson.edu. **Fax:** +1-864-656-7299.

Abbreviations: **EK**, electrokinetic; **EKI**, electrokinetic instability; **JH**, Joule heating

* Additional corresponding author: Prof. Liandong Yu. **E-mail:** liandongyu@upc.edu.cn.

Abstract

Instability occurs in the electrokinetic flow of fluids with conductivity and/or permittivity gradients if the applied electric field is beyond a critical value. Understanding such an electrokinetic instability is significant for both improved transport (via the suppressed instability) and enhanced mixing (via the promoted instability) of liquid samples in microfluidic applications. This work presents the first study of Joule heating effects on electrokinetic microchannel flows with conductivity gradients using a combined experimental and numerical method. The experimentally observed flow patterns and measured critical electric fields under Joule heating effects to different extents are reasonably predicted by a depth-averaged numerical model. It is found that Joule heating increases the critical electric field for the onset of electrokinetic instability because the induced fluid temperature rise and in turn the fluid property change (primarily the decreased permittivity) lead to a smaller electric Rayleigh number.

Keywords

Joule heating; electrokinetic instability; depth-averaged model; micromixing; microfluidics

1 Introduction

Electrokinetic (EK) phenomena refer to the fluid flow (i.e., electroosmosis) and particle motion (i.e., electrophoresis) in response to electric field [1,2]. They have been widely used in microfluidic devices to pump [3], mix [4], trap [5], and separate [6] various types of liquid samples because of the ease, precision and (potentially) autonomy of control [7,8]. This is attributed to the strictly laminar and nearly plug-like EK flow with a linear dependence on electric field [9,10]. However, the action of electric field upon fluid property (in particular, electric conductivity and permittivity) gradients generates an electric body force, which, if sufficiently strong, may destabilize the EK flow [11,12]. One such example is the so-called electrokinetic instability (EKI), which is induced at the interface of the EK co-flow of two fluids with electric conductivity gradients [13]. It is common to encounter two (or more) fluids with dissimilar ionic concentrations (and hence different electric conductivity and/or permittivity values) in microfluidic applications such as electrokinetic displacement [14] and mixing [15] of fluids. Therefore, understanding the principle of EKI becomes significant for both an improved fluid transport via the suppressed EKI and an enhanced fluid mixing via the promoted EKI [16]. This subject has been studied by various research groups using experimental, theoretical and numerical approaches [17-27] since EKI was demonstrated by the Santiago group [28].

However, the effects of Joule heating (JH) on EKI have been ignored in all previous studies. JH is an inevitable phenomenon in EK microfluidic devices [29,30]. It results from the resistance

of the aqueous solution to electric current, which first elevates the fluid temperature and then heats up the entire microchip through thermal diffusion [31,32]. The induced temperature gradients cause non-uniformities to fluid viscosity (and hence species diffusivity), conductivity and permittivity etc. due to their respective strong temperature dependences [33]. The immediate consequence is a significantly increased sample dispersion and in turn a decreased electrophoretic separation of species because of the distorted EK flow profile [3,9,34-36]. Moreover, the interaction between thermally affected fluid properties and electric field leads to a similar electric body force to that in the EKI [37]. The resulting electrothermal flow usually manifests itself in the form of counter-rotating fluid circulations if JH effects are sufficiently strong in, for example, insulator-based dielectrophoretic (iDEP) microdevices because of the locally amplified electric field [38,39]. Such a flow has been found to weaken the dielectrophoretic focusing and trapping of particles [40-44]. It, however, has been recently exploited to achieve a localized enrichment of submicron particles near the insulating tips of a ratchet microchannel [45].

We present in this work a combined experimental and numerical study of JH effects on electrokinetic flows with conductivity gradients. The objective is to understand if and how the thermally modified electric body force may influence the formation and pattern of EKI. We choose the EK co-flow of ferrofluid and water in a T-shaped microchannel as our system, for which the EKI due to the electric conductivity mismatch has been previously investigated by our group with the assumption of negligible JH effects [23,46]. Fluorescent labeling is not required in this system

as the interface between the opaque ferrofluid and transparent water can be directly visualized under a bright-field microscope. The heat transfer condition on the lower substrate of the microchip is varied in order to change the extent of JH effects. We also develop a depth-averaged numerical model to simulate the effects of JH on EKI. The predicted flow patterns and critical electric fields (for the onset of EKI) are compared with the experimental results. Moreover, the concept of electric Rayleigh number, as defined in Chen et al. [16], is borrowed to characterize the JH effects on EKI.

2 Experiment

2.1 Microchip and fluids

A symmetric T-shaped microchannel was used in our experiment. It was fabricated using the standard soft lithography technique, and the procedure was given elsewhere [23]. Figure 1 shows the structure and dimensions of the microchip in both the top and cross-sectional views. Briefly, the microchannel has two 100 μm wide, 8 mm long side-branches that join into a 200 μm wide, 10 mm long main-branch with a measured depth of 50 μm everywhere. It sits at the bottom side of a 3 mm thick polydimethylsiloxane (PDMS) slab, and is sealed with a 1 mm thick glass slide from below. The cylindrical inlet (two) and outlet (one) reservoirs are all through holes in the PDMS slab with the diameters of 5.5 mm and 6.5 mm, respectively. They were made large to reduce the influence of the hydrostatic pressure-driven backflow because of the liquid depletion and buildup in the inlet and outlet reservoirs, respectively, during the run of tests. Ferrofluid was prepared by diluting the original EMG 408 ferrofluid (Ferrotec Corp., 1.2% vol. of 10 nm diameter

magnetic nanoparticles) with deionized water (Fisher Scientific) to four concentrations, namely $0.1\times$, $0.2\times$, $0.3\times$ and $0.4\times$ by volume fraction.

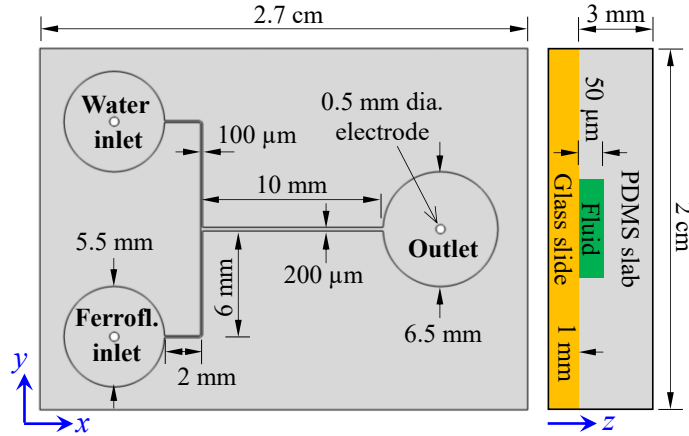


Figure 1. Top (left panel) and cross-sectional (right panel) views (not drawn to scale) of the structure and dimensions of the microchip used in the experiment and simulation.

2.2 Fluid handling

Prior to experiment, all reservoirs were emptied. Equal volume of ferrofluid and water were dispensed to fully fill the two inlet reservoirs, respectively. The outlet reservoir was then completely filled with water to match the liquid height in the inlet reservoirs to remove the pressure-driven flow. Three 0.5 mm diameter platinum wires were used as electrodes that were inserted into the liquid in each reservoir. The two inlet electrodes were connected in parallel to a DC power supply (Glassman High Voltage Inc.) while the outlet electrode was grounded. The flow behavior of the ferrofluid/water interface was visualized at the T-junction of the microchannel using an inverted microscope (Nikon Eclipse TE2000U, Nikon Instruments) under a bright-field illumination. Digital images were recorded through a CCD camera (Nikon DS-Qi1Mc) at a rate of

around 15 frames per second. They were post-processed using the Nikon imaging software (NIS-Elements AR 2.30).

2.3 Variation of the heat transfer condition

The heat transfer condition on the glass slide of the microchip was varied in the experiment to change the extent of JH effects. Specifically, in the *Isothermal* mode, the bottom surface of the glass slide was made to have a good contact with the large flat surface of the microscope stage, and hence can be treated to remain approximately at the room temperature. This approximate treatment has been validated in several recent works through the comparison between experiment and simulation [32,45,46]. In the *Convective* mode, the microchip was lifted up from the microscope stage by the use of a poorly conductive spacer at each end of the glass slide. Hence, the bottom surface of the glass slide can be treated to expose to a natural convection. All other surfaces of the microchip experience a natural convection in both heat transfer modes. Therefore, JH effects are supposed to be stronger in the Convective mode than in the Isothermal mode because of the poorer heat dissipation in the former.

3 Simulation

3.1 Depth-averaged governing equations

The effects of JH on EKI are simulated using a depth-averaged numerical model. The governing equations for the involved electric, temperature, flow, and concentration fields [47,48] are

summarized below. The detailed process for the associated asymptotic analysis [49] is presented in the Supporting Information.

Electric field, \mathbf{E} :

$$\nabla_{\mathbf{H}} \cdot (\sigma \mathbf{E}) = 0 \quad (1)$$

where $\nabla_{\mathbf{H}}$ denotes the vector differential operator in the horizontal plane of the microchip, σ is the electric conductivity of the fluid, and $\mathbf{E} = -\nabla\phi$ with ϕ being the electric potential.

Temperature field, T :

$$\rho C_p \left(\frac{\partial T}{\partial t} + \mathbf{u} \cdot \nabla_{\mathbf{H}} T \right) = \nabla_{\mathbf{H}} \cdot (k \nabla_{\mathbf{H}} T) + \sigma \mathbf{E}^2 - \frac{T - T_{\infty}}{2d} \left(\frac{1}{R_{us}} + \frac{1}{R_{ls}} \right) \quad (2)$$

where ρ , C_p and k are the mass density, heat capacity, and thermal conductivity of the fluid (or PDMS substrate where $\mathbf{E} = \mathbf{0}$), t is the time coordinate, $\mathbf{u} = \mathbf{u}(u, v)$ is the two-dimensional velocity vector in the horizontal plane, T_{∞} is the room temperature, and d is the half-depth of the microchannel. In addition, $R_{us} = th_{PDMS}/k_{PDMS} + 1/h_{ts}$ and $R_{ls} = th_{glass}/k_{glass} + 1/h_{bs}$ are the equivalent thermal resistances of the upper PDMS and lower glass substrates per unit area, where th_{PDMS} and th_{glass} are the thicknesses of the PDMS slab and glass slide, and h_{ts} and h_{bs} are the natural convective heat transfer coefficients of the top and bottom surfaces of the microchip, respectively. The second and third terms on the right hand side of Eq. (2) represent the volumetric JH and surface heat dissipation through the upper/lower substrates of the microchip, respectively. Note that $h_{bs} = \infty$ in the Isothermal mode as described in the **Experiment** section. Also noted is that k_{PDMS} in the definition of R_{us} should be replaced with the fluid thermal conductivity, k_f , in the reservoirs.

Flow field, \mathbf{u} :

$$\nabla_{\mathbf{H}} \cdot \mathbf{u} = 0 \quad (3)$$

$$\rho \left(\frac{\partial \mathbf{u}}{\partial t} + \mathbf{u} \cdot \nabla_{\mathbf{H}} \mathbf{u} \right) = -\nabla_{\mathbf{H}} p + \nabla_{\mathbf{H}} \cdot (\mu \nabla_{\mathbf{H}} \mathbf{u}) + \mathbf{f}_e - \frac{3\mu}{d^2} (\mathbf{u} - \mathbf{u}_{EO}) \quad (4)$$

where p is the hydrodynamic pressure, μ is the fluid viscosity, ε is the fluid permittivity, $\mathbf{f}_e = \nabla_{\mathbf{H}} \cdot (\varepsilon \mathbf{E}) \mathbf{E} - \frac{1}{2} \mathbf{E}^2 \nabla_{\mathbf{H}} \varepsilon$ is the electric body force that consists of the Coulomb and dielectric components [50], and $\mathbf{u}_{EO} = -\varepsilon(\zeta_{PDMS} + \zeta_{glass}) \mathbf{E} / 2\mu$ denotes the average electroosmotic velocity of the top PDMS and bottom glass walls of the microchannel with ζ_{PDMS} and ζ_{glass} being the zeta potentials of the corresponding walls. The last term in Eq. (4) accounts for the influences of the microchannels' top and bottom walls on the EK flow.

Concentration field, c :

$$\frac{\partial c}{\partial t} + \mathbf{u} \cdot \nabla_{\mathbf{H}} c = \nabla_{\mathbf{H}} \cdot (D \nabla_{\mathbf{H}} c) + \frac{2}{105} d^2 \nabla_{\mathbf{H}} \cdot \frac{(\mathbf{u} - \mathbf{u}_{EO})[(\mathbf{u} - \mathbf{u}_{EO}) \cdot \nabla_{\mathbf{H}} c]}{D} \quad (5)$$

where c denotes the concentration of ferrofluid nanoparticles, and D is the diffusion coefficient of ferrofluid nanoparticles. The last term accounts for the influence of the depth-wise fluid velocity.

3.2 Computational domain and boundary conditions

The computational domain covers the full-scale geometry in the horizontal plane of the microchip (see the left panel in Figure 1). It is composed of the fluid sub-domain (within the microchannel/reservoirs) for all the four transport fields, and the PDMS sub-domain for the temperature field only. Figure 2 shows the meshed computational domain (the meshing parameters will be explained in the next section) along with the boundary conditions. For the electric field in

Eq. (1): the two inlet electrodes (each treated as a 0.5 mm diameter hole in the reservoir) are imposed with an equal electric potential $\phi = \phi_{in}$ and the outlet electrode has $\phi = 0$; all walls of the microchannel and reservoirs are electrically insulated. For the temperature field in Eq. (2): all electrodes are assumed to be isothermal at room temperature; the outer surfaces of the PDMS sub-domain are imposed with a natural convection condition. For the flow field in Eqs. (3) and (4): all electrodes have a zero pressure and a non-slip condition; all walls of the microchannel and reservoir are imposed with an electroosmotic slip velocity, $\mathbf{u}_{slip} = -\varepsilon\zeta_{PDMS}\mathbf{E}/\mu$, under the thin electric double layer assumption [1,2]. For the concentration field in Eq. (5): all electrodes and walls are non-penetrating. As to the initial conditions, the temperature of the whole microchip is set to room temperature, and the fluid is set to be motionless. The concentration is set to c_0 and 0 for the ferrofluid and water halves of the fluid sub-domain, where c_0 is the dilution (or volume ratio) of the original ferrofluid (e.g., $c_0 = 0.3$ for 0.3× ferrofluid).

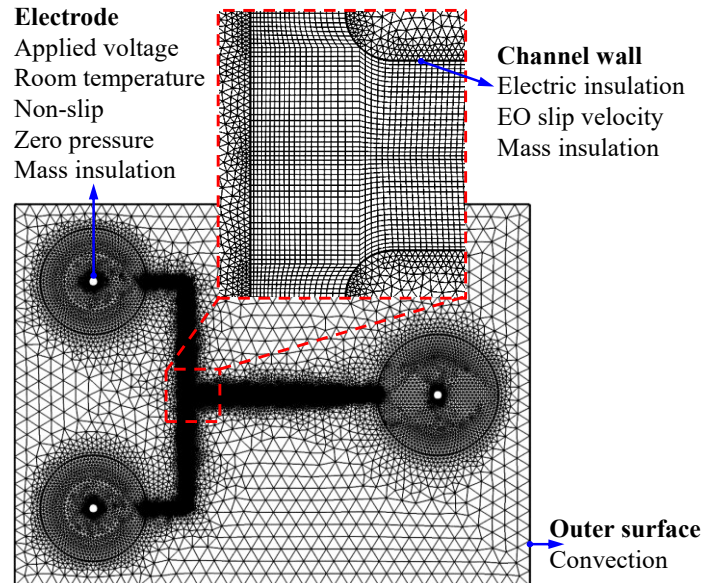


Figure 2. The meshed computational domain and boundary conditions for the depth-averaged numerical model.

3.3 Numerical method and material properties

We used the commercial finite element software, COMSOL[®] 5.4, to develop the depth-averaged model. The governing equations for the electric, temperature, flow, and concentration fields were solved using the “Electric Currents”, “Heat transfer in Fluid”, “Laminar Flow”, and “Transport of Diluted Species” modules, respectively. These equations are coupled through the temperature and concentration dependences of the fluid’s electric conductivity [23,29],

$$\sigma = [c\sigma_{f0} + (1 - c)\sigma_{w0}][1 + \beta(T - T_{\infty})] \quad (6)$$

where σ_{f0} and σ_{w0} are the electric conductivities of the ferrofluid and water at room temperature, and β is the temperature coefficient of electric conductivity. The permittivity and viscosity of the fluid are each treated equal to that of water with the following temperature dependences [39-41],

$$\varepsilon = \varepsilon_0[1 + \alpha(T - T_{\infty})] \quad (7)$$

$$\mu = \left[2.761 \times 10^{-6} \exp\left(\frac{1713}{T}\right) \right] \quad (8)$$

where ε_0 is the fluid permittivity at room temperature with α being the temperature coefficient.

It has been reported in several papers that the magnitude of zeta potential increases with fluid temperature [51-53]. To account for this dependence, we employ the approximation that the product of permittivity and zeta potential, $\varepsilon\zeta$, does not vary with temperature [51] for simplicity.

Other fluid properties including the density and heat capacity are assumed independent of fluid temperature and concentration. The diffusion coefficient of ferrofluid nanoparticles is a function of fluid temperature, $D = D_0(T\mu_0/\mu T_{\infty})$, which is obtained from the Stokes-Einstein equation

with $D_0 = 1 \times 10^{-9} \text{ m}^2/\text{s}$ being the assumed diffusivity at room temperature in order to reduce the influence of numerical dispersion [54,55] and μ_0 the room-temperature viscosity. The values of the material parameters involved in the simulation are summarized in Table S1 of the Supporting Information. The microchannel is meshed with square elements while the reservoirs and PDMS are meshed with triangular elements (see the inset in Figure 2). A grid independence study (see Fig. S1 in the Supporting Information) indicates that 20 elements in the channel half-width is sufficient to ensure the accuracy of our model. Clemson Palmetto Cluster was used to solve the model.

4 Results and discussion

4.1 JH effects on the concentration field

Figure 3 compares the experimentally and numerically obtained concentration fields in the EK co-flow of $0.3\times$ ferrofluid and water at the T-junction of the microchannel for the Isothermal and Convective modes, respectively. All images are obtained 20 s after the electric field is applied. In the Isothermal mode, no instability waves are observed at the interface of ferrofluid and water in the experiment until the applied electric field is increased to 150.0 V/cm (termed the critical electric field for the onset of EKI, calculated from the imposed 270 V voltage drop across the overall 1.8 cm long channel). Further increasing the electric field enhances the EKI and can generate chaotic waves under the electric field of 194.4 V/cm (and more) in the experiment. In contrast, the periodic EKI waves do not occur in the Convective mode until a higher electric field

of 169.4 V/cm (corresponding to 305 V voltage drop, 13% greater than in the Isothermal mode) is reached in the experiment. They remain stable but become apparently stronger with a greater wave amplitude when the electric field is increased to 194.4 V/cm. The experimentally obtained interfacial behaviors are reasonably simulated by the depth-averaged numerical model for both heat transfer modes in Figure 3. Moreover, the predicted critical electric fields of 162.5 and 179.2 V/cm for the onset of EKI closely match the experimental data, i.e., 150.0 and 169.4 V/cm, in the Isothermal and Convective modes with an error of 8.3% and 5.7%, respectively. As we will show in the next section, JH effects are much stronger in the Convective mode. Therefore, the observed increase in critical electric field from the Isothermal to the Convective mode indicates a suppressing effect of JH on EKI.

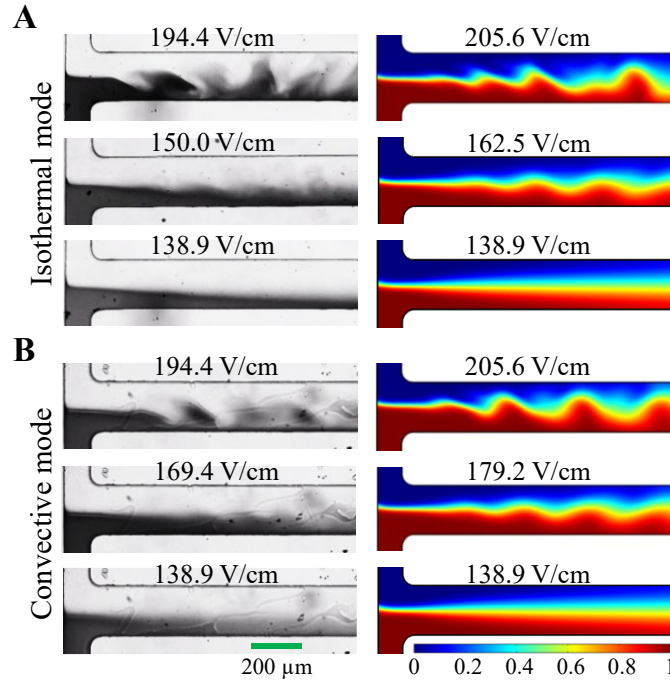


Figure 3. Experimental (left column) and numerical (right column) images of the concentration field in the EK co-flow of 0.3x ferrofluid and water at the T-junction of the microchannel in the

Isothermal (A) and Convective (B) modes. The experimental and numerical images are all obtained 20 s after the indicated electric field is applied.

4.2 JH effects on other fields

To understand why JH stabilizes the EK flow, we further use the depth-averaged model to investigate the other transport fields as well as the fluid property fields in the flow of $0.3\times$ ferrofluid and water for both the Isothermal and Convective modes. The greater critical electric field of 179.2 V/cm for the Convective mode is selected for the demonstration. All images are again obtained 20 s after the application of electric field. Figure 4 compares the predicted temperature contours in the whole microchip in between the two heat transfer modes. The temperature increase is minimal in the Isothermal mode (with a maximum value of 0.8 °C only) as expected because of the quick heat dissipation through the isothermal glass slide that acts as a heat sink. In contrast, significant temperature rise occurs in the Convective mode in both the ferrofluid side-branch (where the maximum increase of 16.2 °C occurs) and the main-branch. This is because the JH generated in the highly conductive ferrofluid (both before and after the mixing with water in the main-branch) cannot be effectively dissipated through a purely natural convection. Therefore, strong temperature gradients are formed in the fluid, particularly at the T-junction of the microchannel where the cold water and hot ferrofluid first meet (see the inset on the bottom panel of Figure 4).

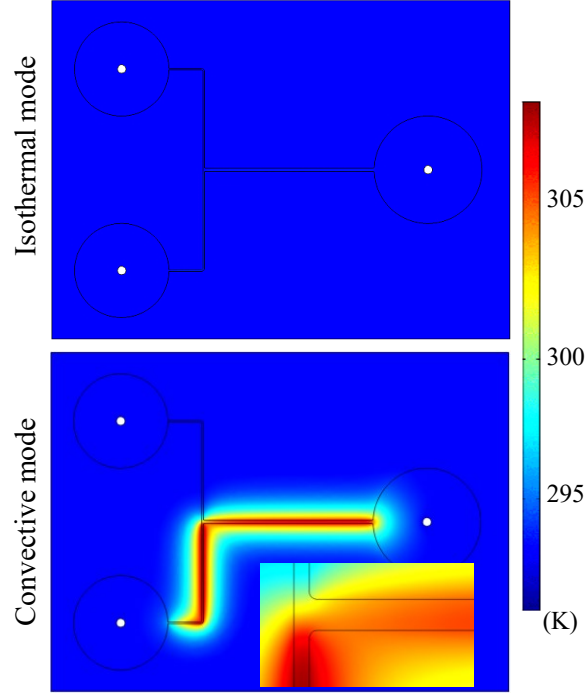


Figure 4. Numerically predicted temperature field in the entire microchip for the EK co-flow of 0.3x ferrofluid and water in the Isothermal (upper panel) and Convective (lower panel) modes. Both images are obtained 20 s after the critical electric field of 179.2 V/cm for the Convective mode is applied. The inset on the lower panel shows the zoom-in view of the temperature contour at the T-junction of the microchannel.

As a consequence of the greater temperature elevation in the Convective mode, the electric conductivity of the ferrofluid (in both the side-branch and main-branch) becomes significantly larger than in the Isothermal mode as seen from the conductivity contours in Figure 5A. This leads to a slightly smaller electric field in the main-branch in the Convective mode because of the conservation of electric current. Moreover, the electric field gradient in the main-branch also gets weaker than in the Isothermal model as illustrated by the electric field contours and lines in Figure 5B. These variations along with the JH induced decrease in fluid permittivity (Figure 5C) cause an apparently smaller electric body force, \mathbf{f}_e , in the Convective mode (see the length of the vector arrows in Figure 5D). Therefore, the fluid velocity in the Convective mode exhibits a more

homogeneous pattern (Figure 5E), though at a higher magnitude than in the Isothermal mode because of the JH induced decrease in fluid viscosity (Figure 5F). Another property of significance to EKI is the diffusion coefficient, which, as seen from the contour in Figure 5G, increases with JH effects and hence becomes larger in the Convective mode.

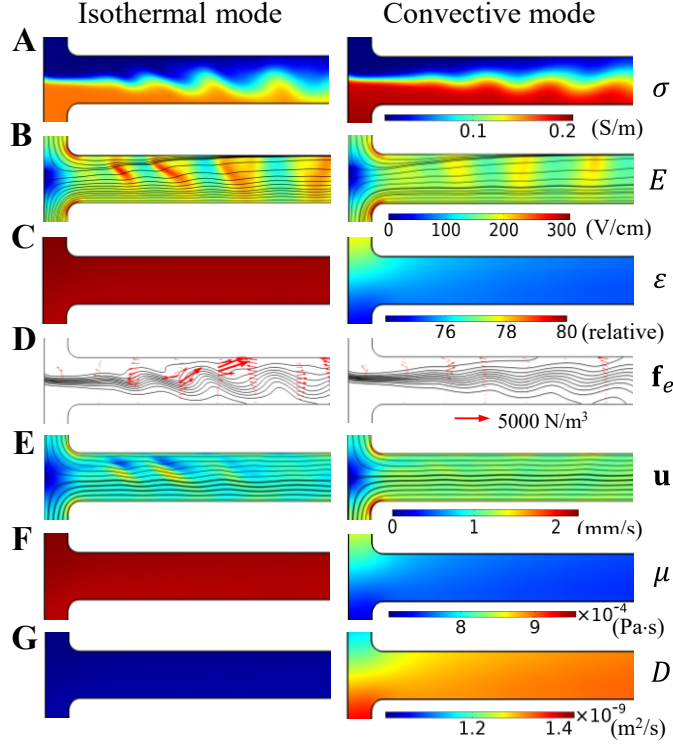


Figure 5. Numerically predicted fluid transport and property fields for the EK co-flow of $0.3\times$ ferrofluid and water in the Isothermal (left column) and Convective (right column) modes: (A) electric conductivity contour, (B) electric field contour and lines, (C) relative permittivity contour, (D) electric body force vectors (the background shows the contour lines of ferrofluid concentration), (E) velocity contour and lines, (F) viscosity contour, and (G) diffusivity contour. All images are obtained 20 s after the critical electric field of 179.2 V/cm for the Convective mode is applied.

The effects of JH on EKI via the fluid temperature rise and as well the temperature-induced fluid property variations can be characterized by the electric Rayleigh number, which, as defined by Chen et al. [16], is written as,

$$Ra_e = \Gamma \frac{\varepsilon E^2 d^2}{\mu D} \quad (9)$$

where $\Gamma = (\gamma - 1)^2 / (\gamma + 1)^2$ with γ being the conductivity ratio between the high and low conductivity fluids, and the diffusion length in the original definition has been assumed equal to the channel half-width for simplicity. As discussed by Chen et al. [16], Ra_e controls the onset of convective EKI. Considering the dependence of diffusion coefficient on the fluid viscosity in the Stokes-Einstein equation, we may rewrite Eq. (9) as follows,

$$Ra_e = 6\pi\Gamma \frac{ad^2}{k_B} \frac{\varepsilon E^2}{T} \quad (10)$$

where $a = 5$ nm is the radius of ferrofluid nanoparticles, and k_B is the Boltzmann constant. As JH causes an increase in the fluid temperature and in turn a decrease in the fluid permittivity and electric field, the value of Ra_e decreases requiring a higher electric field to drive the EKI. This will, however, further strengthen the JH effects and hence render an even higher electric field for the onset of EKI, which may imply the cessation of EKI under a sufficiently strong JH. In other words, JH has a stabilizing effect on the EK flow, which is consistent with a previous theoretical analysis [56].

4.3 JH effects at varying ferrofluid concentrations

Figure 6A shows the effect of ferrofluid concentration on the critical electric field for the onset of EKI in both the Isothermal and Convective modes. JH effects are insignificant in the Isothermal mode, for which the experimentally measured critical electric field decreases with the increase of ferrofluid concentration. This trend is consistent with previous studies [16,23,47] because of the

enhanced electric conductivity ratio and hence increased Γ in the definition of Ra_e . In contrast, the experimentally measured critical electric field in the Convective mode shows a first decrease and then increase trend in Figure 6A when the ferrofluid concentration is increased from $0.1\times$ to $0.4\times$. This is because the JH effects become increasingly strong as illustrated by the predicted higher fluid temperature in Figure 6B, which along with the decreased fluid permittivity may counter-balance the enhanced conductivity ratio necessitating a higher critical electric field. The observed variation of critical electric field with ferrofluid concentration is properly simulated in both heat transfer modes. The slight over-prediction (less than 15% for all cases illustrated in Figure 6A) is believed to result from the simple averaging of the governing equations in the channel depth direction, which, as pointed out in our earlier paper [47], tends to overly consider the stabilizing effect from the top/bottom walls.

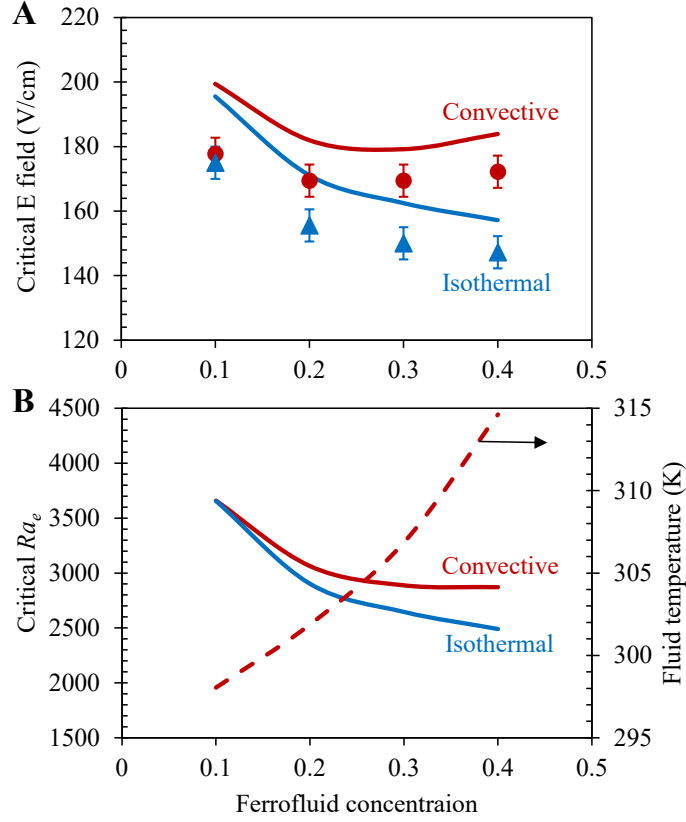


Figure 6. Effect of ferrofluid concentration on the EK co-flow of ferrofluid and water in the Isothermal and Convective modes: (A) experimentally (symbols with error bars) and numerically (solid lines) obtained critical electric field for the onset of EKI; (B) predicted critical electric Rayleigh number Ra_e (solid lines) and fluid temperature (averaged over the channel width in the middle of the main-branch for the Convective mode only, dashed line). Note that the average fluid temperature in the Isothermal mode is less than 294 K in all cases and hence not shown in (B).

Figure 6B also shows the plot of the critical Ra_e for the onset of EKI, which is calculated using Eq. (10) with the numerically predicted critical electric field and the corresponding fluid temperature. The value of the critical Ra_e in the Convective mode is larger than that in the Isothermal mode at each ferrofluid concentration, which matches the relationship for the critical electric field. However, the relative difference between the predicted critical Ra_e in the two heat transfer modes remains marginal, and increases from (nearly) 0% in 0.1× ferrofluid to around 15% in 0.4× ferrofluid. The absolute value of the critical Ra_e in each heat transfer mode decreases

with the increase of ferrofluid concentration, or alternately the conductivity ratio. This trend appears to be consistent with the observation of Chen et al. [16]. Moreover, similar to the analysis of both Chen et al. [16] and Navaneetham & Posner [21], our predicted onset conditions for EKI in all the tested ferrofluids seem to not deviate significantly from a critical Ra_e of approximately 2500.

5 Concluding remarks

We have conducted a combined experimental and numerical study of JH effects on the electrokinetic flow of ferrofluid and water through a T-shaped microchannel. The extent of JH is varied by changing the heat transfer condition on the bottom surface of the microchip from Isothermal to Convective. The critical electric field for the onset of EKI in the Convective mode is found to be higher than that in the Isothermal mode at each concentration of the ferrofluids tested because of the impact of the thermally modified electric body force. Moreover, it exhibits a non-monotonic variation with the increase of ferrofluid concentration, dissimilar to the decreasing trend in the Isothermal mode. These differences result from the stronger JH effects in the Convective mode that cause both a higher temperature rise in the fluid and a greater change of fluid properties. We have also developed a depth-averaged numerical model, which proves sufficient to predict the observed EK flow patterns and critical electric fields in all cases with a reasonable agreement. Moreover, we have used the electric Rayleigh number, Ra_e , to explain the effects of JH on EKI.

It is primarily the combination of the increased temperature and decreased permittivity of the fluid that causes a reduction of Ra_e and hence requires a higher electric field to render EKI.

Data Availability Statement

The data that support the findings of this study are available from the corresponding author upon reasonable request.

This work was supported in part by China Scholarship Council (CSC) - Chinese Government Graduate Student Overseas Study Program (L.S.), University 111 Project of China under grant number B12019 (L.Y.), Clemson University through the Departmental Honors Research Program and Creative Inquiry Program (X.X.), and NSF under grant number CBET-1704379 (X.X.).

The authors have declared no conflict of interest.

6 References

- [1] Li, D. *Electrokinetics in microfluidics*, Elsevier Academic Press, Burlington, MA (2004).
- [2] Chang, H. C., Yeo, L. Y., *Electrokinetically Driven Microfluidics and Nanofluidics*, Cambridge University Press, New York (2010).
- [3] Ghosal, S., *Electrophoresis* 2014, 25, 214-228.
- [4] Chang, C. C., Yang, R. J. *Microfluid. Nanofluid.* 2007, 3, 501-525.

- [5] Regtmeier, J., Eichhorn, R., Viefhues, M., Bogunovic, L., Anselmetti, D., *Electrophoresis* 2011, 32, 2253-2273.
- [6] Xuan, X., *Electrophoresis* 2019, 40, 2484-2513.
- [7] Zhao, C., Yang, C. *Microfluid. Nanofluid.* 2012, 13, 179-203.
- [8] Lapizco-Encinas, B. H., *Electrophoresis* 2019, 40, 358-375.
- [9] Ghosal, S., *Annu. Rev. Fluid Mech.* 2006, 38, 309-338.
- [10] Whitesides, G. M., Stroock, A. D., *Phys. Today* 2001, 54, 42-48.
- [11] Saville, D. A., *Annual. Rev. Fluid Mech.* 1997, 29, 27-64.
- [12] Casterllanos, A., Ramos, A., Gonzalez, A., Green, N. G., Morgan, H., *J. Phys. D*, 2003, 36, 2584-2597.
- [13] Lin, H., *Mech. Res. Comm.* 2009, 36, 33-38.
- [14] Bahgaa, S. S., Santiago, J. G., *Analyst* 2013, 138, 735-754.
- [15] Lee, C. Y., Chang, C. L., Wang, Y. N., Fu, L. M., *Int. J. Mol. Sci.* 2011, 12, 3263-3287.
- [16] Chen, C., Lin, H., Lele, S. K., Santiago, J. G., *J. Fluid Mech.* 2005, 524, 263-303.
- [17] Kang, K. H., Park, J., Kang, I. S., Huh, K. Y., *Int. J. Heat Mass Trans.* 2006, 49, 4577-4583.
- [18] Boy, D. A., Storey, B. D., *Phys. Rev. E* 2007, 76, 026304.
- [19] Lin, H., Storey, B. D., Santiago, J. G., *J. Fluid Mech.* 2008, 608, 43-70.
- [20] Luo, W. J., *Microfluid. Nanofluid.* 2009, 6, 189-202.
- [21] Navaneetham, G., Posner, J. D., *J. Fluid Mech.* 2009, 619, 331-365.

- [22] Posner, J. D., Perez, C. L., Santiago, J. G., *Proc. Natl. Acad. Sci.* 2012, *109*, 14353-14356.
- [23] Kumar, D. T., Zhou, Y., Brown, V., Lu, X., Kale, A., Yu, L., Xuan, X., *Microfluid. Nanofluid.* 2015, *19*, 43.
- [24] Li, Q., Delorme, Y., Frankel, S. H., *Microfluid. Nanofluid.* 2016, *20*, 29.
- [25] Dubey, K., Gupta, A., Bahga, S. S., *Phys. Fluid.* 2017, *29*, 092007.
- [26] Song, L., Jagdale, P., Yu, L., Liu, Z., Zhang, C., Gao, R., Xuan, X., *Microfluid. Nanofluid.* 2018, *22*, 134.
- [27] Song, L., Jagdale, P., Yu, L., Liu, Z., Li, D., Zhang, C., Xuan, X., *Phys. Fluid.* 2019, *31*, 082001.
- [28] Lin, H., Storey, B. D., Oddy, M. H., Chen, C., Santiago, J. G., *Phys. Fluid.* 2004, *16*, 1922-1935.
- [29] Xuan, X., *Electrophoresis* 2008, *29*, 33-43.
- [30] Cetin, B., Li, D., *Electrophoresis* 2008, *29*, 994-1005.
- [31] Nakano, A., Luo, J., Ros, A., *Anal. Chem.* 2014, *86*, 6516-6524.
- [32] Gallo-Villanueva, R. C., Perez-Gonzalez, V. H., Cardenas-Benitez, B., Jind, B., Martinez-Chapa, S. O., Lapizco-Encinas, B. H., *Electrophoresis* 2019, *40*, 1408-1416.
- [33] Rathore, A. S., *J. Chromatography A* 2004, *1037*, 431-443.
- [34] Gas, B., *J. Chromatography A* 1993, *644*, 161-174.
- [35] Xuan, X., Li, D., *Electrophoresis* 2005, *26*, 166-175.

- [36] Tang, G., Yan, d., Yang, C., Gong, H., Chai, J. C., Lam, Y. C., *Electrophoresis* 2006, 27, 628-639.
- [37] Green, N. G., Ramos, A., Morgan, H., *J. Phys. D* 2000, 33, 632-641.
- [38] Hawkins, B. J., Kirby, B. J., *Electrophoresis* 2010, 31, 3622–3633.
- [39] Sridharan, S., Zhu, J., Hu, G., Xuan, X., *Electrophoresis* 2011, 32, 2274-2281.
- [40] Kale, A., Patel, S., Hu, G., Xuan, X., *Electrophoresis* 2013, 34, 674-683.
- [41] Kale, A., Patel, S., Qian, S., Hu, G., Xuan, X., *Electrophoresis* 2014, 35, 721-727.
- [42] Chaurey, V., Rohani, A., Su, Y. H., Liao, K. T., Chou, C. F., Swami, N. S., *Electrophoresis* 2013, 34, 1097-1104.
- [43] Gallo-Villanueva, R., Sano, M., Lapizco-Encinas, B., Davalos, R., *Electrophoresis* 2014, 35, 352-361.
- [44] Wang, Q., Dingari, N. N., Buie, C. R., *Electrophoresis* 2017, 38, 2576-2586.
- [45] Kale, A., Song, L., Lu, X., Yu, L., Hu, G., Xuan, X., *Electrophoresis* 2018, 39, 887-896.
- [46] Zehavi, M., Boymelgreen, A., Yossifon, G., *Phys. Rev. Appl.* 2016, 5, 044013.
- [47] Song, L., Yu, L., Zhou, Y., Antao, A. R., Prabhakaran, R. A., Xuan, X., *Sci. Rep.* 2017, 7, 46510. doi: 10.1038/srep46510
- [48] Prabhakaran, R. A., Zhou, Y., Patel, S., Kale, A., Song, Y., Hu, G., Xuan, X., *Electrophoresis* 2017, 38, 572-579.
- [49] Lin, H., Storey, B. D., Santiago, J. G., *J. Fluid Mech.* 2008, 608, 43-70.
- [50] Melcher, J. R., Taylor, G. I., *Annual Rev. Fluid Mech.* 1969, 1, 111-146.

- [51] Petersen, N. J., Nikolajsen, R. P. H., Mogensen, K. B., Kutter, J. P., *Electrophoresis* 2004, 25, 253-269.
- [52] Venditti, R., Xuan, X., Li, D., *Microfluid. Nanofluid.* 2006, 2, 493-499.
- [53] Evenhuis, C. J., Guijt, R. M., Macka, M., Marriott, P. J., Haddad, P. R., *Electrophoresis* 2006, 27, 672-676.
- [54] Wen, C.-Y., Liang, K.-P., Chen, H., Fu, L.-M., *Electrophoresis* 2011, 32, 3268–3276.
- [55] Zhu, G., Nguyen, N. T., *Microfluid. Nanofluid.* 2012, 13, 655–663.
- [56] Chang, M.-H. Homsy, G. M., *Phys. Fluids* 2005, 17, 074107.